Constraints on Paleoproterozoic atmospheric oxygen levels

Eric J. Bellefroid[a,1], Ashleigh v. S. Hood[a], Paul F. Hoffman[b,1], Matthew D. Thomas[a], Christopher T. Reinhard[c,d], and Noah J. Planavsky[a,d]

[a]Department of Geology and Geophysics, Yale University, New Haven, CT 06511; [b]School of Earth and Ocean Sciences, University of Victoria, Victoria, BC, V8P 3E6 Canada; [c]School of Earth and Atmospheric Sciences, Georgia Tech, Atlanta, GA 30332; and [d]NASA Astrobiology Institute Alternative Earths Team, University of California, Riverside, CA, 92521

Contributed by Paul F. Hoffman, May 25, 2018 (sent for review April 19, 2018; reviewed by Lee Kump and Rachel A. Wood)

The oxygenation of Earth's surface environment dramatically altered key biological and geochemical cycles and ultimately ushered in the rise of an ecologically diverse biosphere. However, atmospheric oxygen partial pressures (pO_2) estimates for large swaths of the Precambrian remain intensely debated. Here we evaluate and explore the use of carbonate cerium (Ce) anomalies (Ce/Ce*) as a quantitative atmospheric pO_2 proxy and provide estimates of Proterozoic pO_2 using marine carbonates from a unique Precambrian carbonate succession—the Paleoproterozoic Pethei Group. In contrast to most previous work, we measure Ce/Ce* on marine carbonate precipitates that formed in situ across a depth gradient, building on previous detailed sedimentology and stratigraphy to constrain the paleo-depth of each sample. Measuring Ce/Ce* across a full platform to basin depth gradient, we found only minor depleted Ce anomalies restricted to the platform and upper slope facies. We combine these results with a Ce oxidation model to provide a quantitative constraint on atmospheric pO_2 1.87 billion years ago (Ga). Our results suggest Paleoproterozoic atmospheric oxygen concentrations were low, near 0.1% of the present atmospheric level. This work provides another crucial line of empirical evidence that atmospheric oxygen levels returned to low concentrations following the Lomagundi Event, and remained low enough for large portions of the Proterozoic to have impacted the ecology of the earliest complex organisms.

Ce anomalies | rare earth elements | oxygenation | Ce oxidation | Proterozoic

Reconstructing Earth's oxygenation has been the focus of an ongoing surge of research as geologists and paleontologists attempt to understand the environmental factors driving early biotic evolution (1–5) and astrobiologists look to the early Earth to evaluate oxygen as a potential exoplanet "bio-signature" (6). Emerging records suggest that despite the likely evolution of oxygenic photosynthesis in the Archean (7, 8) (or perhaps as late as the Paleoproterozoic; e.g., ref. 9), Earth's atmosphere and surface ocean remained poorly oxygenated for most of their history (10, 11). However, while relatively robust constraints have been placed on Archean and Phanerozoic oxygen levels (12–14), there remain large uncertainties and extensive debate about atmospheric oxygen levels throughout the Proterozoic. Low atmospheric pO_2 levels have been proposed for the Proterozoic based on geochemical proxies tracking terrestrial Fe and Mn mobility (4, 8, 15–17). However, recent work has questioned these low estimates, presenting geochemical data interpreted to reflect higher pO_2 (2, 18). In all cases, quantitative estimates of atmospheric pO_2 during the Proterozoic have been met with controversy (19, 20). Given this debate, as well as potential uncertainties with all current methods, there is a clear need for new approaches toward tracking absolute pO_2 values through the Proterozoic.

To tackle this problem, we have generated a unique Paleoproterozoic marine carbonate cerium (Ce) anomaly record (Ce/Ce*) and propose a means of extrapolating atmospheric pO_2 estimates from these measurements. The behavior of rare earth elements and yttrium (REE+Y), including redox-sensitive Ce, has been well characterized in modern environments and represents a promising tool for paleo-redox work (21–24). In contrast to neighboring REE+Y, Ce is progressively oxidized from soluble Ce(III) to insoluble Ce(IV) in oxic and suboxic conditions (25), leading to Ce depletions relative to non-redox-sensitive neighboring REE+Y. In anoxic conditions, however, Ce(IV) is rapidly reduced and redissolved. Thus, depleted Ce anomalies [Ce/Ce* <1.0, measured as Ce/Ce* = Ce/(Pr^2/Nd) and normalized to post-Archean Australian shale] (26) provide a reliable indication of locally oxic conditions on a basin scale. Measured in marine carbonates, petrographically and geochemically screened samples have been demonstrated to provide a relatively robust Ce/Ce* record, preserving primary seawater values even after recrystallization or dolomitization (27–31).

Recent Proterozoic compilations of marine carbonate Ce/Ce* have shown that, although the majority of studied sequences preserve Ce/Ce* values near 1, depleted Ce/Ce* signatures (<1.0) are found throughout the record, suggesting the persistence of some marine oxic environments within a dominantly anoxic Proterozoic ocean (3, 32). However, while this initial work has provided key insights into the utility of the tool and best practices for measuring it (3, 27, 28, 31), prior work only provides a qualitative view of Proterozoic oxygenation. To more directly estimate dissolved O_2 concentrations, and by extension atmospheric pO_2, a number of challenges must be confronted. First, modern anoxic basins show Ce/Ce* gradients with depth (22), such that paleo-redox reconstructions based on Ce/Ce* must provide a means to constrain the water depth at which carbonate precipitation

Significance

Earth's protracted oxygenation significantly transformed global biological and geochemical cycles. In particular, the rise of atmospheric oxygen above trace levels was an essential prerequisite for the development of animals. However, quantifying atmospheric oxygen levels in Earth's middle age remains a daunting challenge. Here we use a combination of sedimentology, geochemical constraints, and oceanographic modeling to provide a quantitative estimate of Precambrian atmospheric oxygen. We provide evidence that atmospheric oxygen levels decreased significantly after the "Great Oxygenation Event" in Earth's early history, to levels that would have negatively impacted the ecology of the earliest complex organisms.

Author contributions: E.J.B., A.v.S.H., P.F.H., and N.J.P. designed research; E.J.B., A.v.S.H., P.F.H., M.D.T., C.T.R., and N.J.P. performed research; E.J.B., A.v.S.H., and M.D.T. contributed new reagents/analytic tools; E.J.B., A.v.S.H., M.D.T., and C.T.R. analyzed data; and E.J.B. and N.J.P. wrote the paper.

Reviewers: L.K., Pennsylvania State University; and R.A.W., University of Edinburgh.

The authors declare no conflict of interest.

[1]To whom correspondence may be addressed. Email: eric.bellefroid@yale.edu or paulfhoffman@gmail.com.

This article contains supporting information online at www.pnas.org/lookup/suppl/doi:10.1073/pnas.1806216115/-/DCSupplemental.

Published online July 23, 2018.

occurred. Furthermore, Ce oxidation is a kinetically inhibited process (25, 33), with the result that water column Ce/Ce* values reflect a combination of both local dissolved O_2 and Ce residence time within a shallow surface oxic zone. Atmospheric pO_2 estimates based on Ce/Ce* must adequately model upper ocean mixing rates and the depth of the chemocline. Last, the best carbonate components for REE+Y analysis are derived from petrographically well-preserved marine cements and microbialites (3, 27, 28, 30), but the bulk of prior early- and mid-Proterozoic Ce/Ce* data has little petrographic or sedimentological context.

To expand the utility of the Ce anomaly as a paleo-redox proxy and more directly constrain the size of the shallow oxic water mass in relation to atmospheric O_2 levels, we measured Ce/Ce* values across a single well-constrained basinal depth gradient. We targeted the Paleoproterozoic Pethei Group in northern Canada, a carbonate platform primarily composed of well-preserved marine cements and microbial limestones (34). The foreland basin succession preserves a complete platform to basin transect over a broad paleo-depth range (35–38), offering the opportunity to measure marine Ce/Ce* values on in situ sea-floor precipitates and place a depth estimate for each petrographically screened measurement. Using these sedimentological and geochemical results to constrain the depth of the chemocline, we then used a high-resolution coupled general circulation model to estimate surface ocean mixing rates at different potential chemocline depths and coupled these results with a Ce oxidation model to estimate peak Ce/Ce* values across a range of atmospheric oxygen partial pressures. Critically, this work provides an independent test of existing Proterozoic pO_2 estimates.

The Paleoproterozoic Pethei Group

The ∼420-m thick, ∼1.87-Ga Pethei Group is an exceptionally well-preserved carbonate succession widely exposed around the east arm of Great Slave Lake in the Northwest Territories, Canada (35, 36, 39, 40). Deposited on the southeastern Slave Craton margin, the Pethei Group is part of a wedge-shaped foreland basin developed during dextral-oblique collisional indentation of the Slave craton into the Rae craton. The succession is imbricated by refolded brittle thrust nappes, but most stratigraphic sections (except basinal section SL-8; Fig. 1) used in this study are autochthonous with respect to the Slave craton (41–43). The Compton Intrusive Suite, which intrudes the Pethei Group, provides a minimum age constraint of 1,865 ± 15 million years ago (Ma) (44). Radiometric detrital zircon ages on volcanoclastic units of the Kluziai Formation (Fm.) (Sosan Group), overlying the Pethei Group, provide a maximum age constraint of 1,883 ± 10 Ma (45). A similar age of 1,882.5 ± 0.95 Ma for a tuff in the correlative Fontano Fm. (Recluse Group) (46–48) corroborates these age constraints, thus suggesting an age for the basin between 1.88 and 1.87 Ga.

The Pethei Group preserves a north-to-south facies change from outer platform to slope and basin-plain environments (35–37). These facies are unambiguously coeval since the group is bounded above and below by the same marine formations in all facies (*SI Appendix*, Fig. S1). The outer platform aggraded in two stages, the younger of which prograded 3–15 km basin-ward of the older. Both stages first developed stromatolitic reefal rims (Taltheilei and Wildbread formations) and ended with ramps (Utsingi and Hearne formations). The reefal rims exhibit a "spur-and-groove" morphology, oriented normal to the slope break, and had several meters of synoptic relief. The "spurs" are stromatolitic buildups (*SI Appendix*, Fig. S2*C*), a few decameters in width, separated by "grooves" filled with intraclast or less common ooid grainstones (*SI Appendix*, Fig. S2*E*). The spur-and-groove tract passes northward into cyclic stromatolite biostromes, sea-floor cements (*SI Appendix*, Fig. S2*A*), and sheets of wave-ripple ooid grainstone (*SI Appendix*, Fig. S2*F*). The ramps are dominated by "cuspate" microbialites (41) with horizons of formerly aragonitic sea-floor cement (*SI Appendix*, Fig. S2 *B* and *D*). These units lack clear exposure surfaces, suggesting a subtidal paleo-environment. However, they contain ample high-energy indicators, including wave-rippled oolite (*SI Appendix*, Fig. S2*F*) and intraclast grainstones (*SI Appendix*, Fig. S2*E*), oncoid intraclasts (*SI Appendix*, Fig. S2*A*), edgewise conglomerates, and current shaped stromatolites (49). These features likely point toward a subaqueous high-energy platform environment, above fair-weather wave base (<20 m depth; *SI Appendix*, Fig. S2) (35–37).

The slope facies is represented by the McLean and (younger) Pekanatui Point formations (*SI Appendix*, Fig. S1). The McLean Formation is dominated by cuspate microbialite (ref. 41 and *SI Appendix*, Fig. S3), which becomes increasingly argillaceous basin-ward (*SI Appendix*, Fig. S3). The Pekanatui Point Formation consists of finely bedded, laminated, or nodular bedded limestone and silty limestone (40–42). The McLean Formation is locally cut

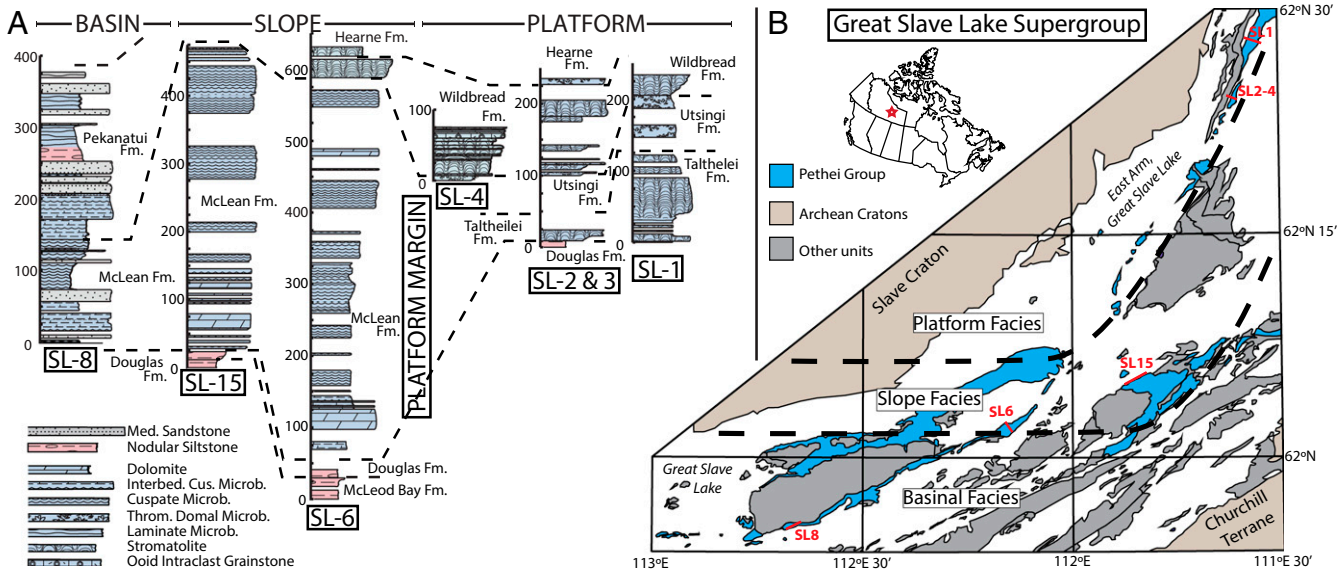

Fig. 1. The east arm of Great Slave Lake, northern Canada, preserves a complete platform to deeper basinal facies transect across the Pethei Group (*A* and *B*). We measured 15 sections across the Pethei Group and selected seven well-preserved and representative sections (*A*) for geochemical analysis. (*B*) Map modified from Hoffman (35, 39). Please refer to *SI Appendix*, Fig. S1 for more detailed stratigraphic sections. Med. Sandstone, medium sandstone; Interbed. Cus. Microb., Cuspate Microbialite interbedded with calcareous siltstone; Microb., Microbialite; Throm. Domal Microb., Thrombolitic Domal Microbialite.

by neptunian dykes (*SI Appendix*, Fig. S3*B*), which are lined by fibrous carbonate cement and internally filled by (structurally tilted) micritic sediment. We relate the fractures to syn-sedimentary slope-induced tensile failure in well-cemented shelf margin lithologies. The fractures cut cleanly across cemented cuspate microbialite and, in turn, are lined with microbial laminae, further fibrous cements, and internal sediment, demonstrating syn-sedimentary marine cementation. Stromatolitic bioherms and microbial lithologies are thicker and more dominant at the platform margin and across the upper slope (e.g., Section SL-6, Fig. 1), whereas carbonate turbidite-dominated facies increase in more distal basinal sections. Abundant microbialite bioherms (several meters in scale) separated by microbial intraclast grainstone channels indicate a shelf-margin environment (35–37), likely above the storm-wave base (<100 m) (Fig. 1).

The basin facies (section SL-8) is structurally allochthonous, and the slope–basin boundary in Fig. 1 is displaced northward, relative to the platform and slope sections, by a minimum of 14 km (44). The basinal sequence is similar to the slope sequence, but with the addition of four intervals (Blanchet Formation; *SI Appendix*, Fig. S1) containing turbidites composed of sand-size greywacke (feldspathic-lithic wacke). The greywacke turbidites are graded Bouma A-E depositional units, typically 10–30 cm in thickness, and eastward-directed climbing ripples suggest a source in Wopmay orogen, 150 km to the west (50). The well-organized, nonchannelized nature of the turbidite units suggests a toe-of-slope submarine fan or axial basin-plain setting, likely in water depths of several hundreds of meters. Deep water is required to provide a submarine slope of sufficient magnitude for the generation of far-traveled, nonchannelized, turbidity currents capable of transporting sand. Poorly developed cuspate microbialite (McLean Formation) occurs between individual turbidites of the older greywacke-rich intervals, and laminated limestone (Pekanatui Point Formation) occurs between turbidites of the younger intervals. The slope and basin facies are therefore internally time equivalent.

A sequence stratigraphic interpretation of the Pethei Group is given in ref. 42. Detailed studies (39, 41, 42) greatly amplified but did not change the original platform–slope–basin facies paleoenvironmental interpretation (40, 46). Overall, all facies of the Pethei platform preserve an abundance of syn-sedimentary precipitated carbonate phases (*SI Appendix*, Fig. S4), which may be microbially influenced precipitates or abiotic marine cements (34). This distribution of volumetrically important in situ carbonate precipitation across a platform and into deeper waters is unusual compared with Phanerozoic platforms, but provides a means to measure seawater conditions at the sea floor on a broad range of paleo-water depths (30, 38, 51), making this basin ideal for determining Paleoproterozoic environmental conditions.

Sample Screening

Precambrian marine carbonates can be relatively poorly preserved compared with younger lithologies; therefore, we selected and screened samples using well-established best practices (3, 30, 52). We found that Pethei Group carbonate lithologies range from well preserved (i.e., depositional fabrics are clearly defined and preserved in fibrous, or relatively finely crystalline calcite) to poorly preserved (i.e., destructively dolomitized or coarsely crystalline), making petrographic and geochemical screening essential. We preferentially targeted marine-cemented microbialite laminae and early fibrous marine cements, which did show some evidence of recrystallization but were generally the best-preserved phases. Cements are composed of cloudy, brown nonluminescent calcite with a fibrous to blocky habit and vestiges of sweeping extinction, characteristic of a primary calcite mineralogy (likely either high-Mg or herringbone calcite), as opposed to secondary late-stage calcite (*SI Appendix*, Figs. S5 and S6). Microbialite laminae are commonly stylolitized and composed of bright to dull luminescent, rhombic dolomite with silicate detritus, all features that were avoided during sampling. We also avoided late-stage calcite burial cements, which occur throughout the basin and are clear in plane light and well zoned under cathodoluminescence, showing non–bright-dull zonation.

Targeted samples were measured for major, trace, and rare earth elements using both a bulk-rock sequential leaching method (52) and laser-ablation inductively coupled plasma mass spectrometer (ICP-MS). Whole-rock carbonate sequential leaching methods allow thorough separation of the least-altered carbonate fractions from detrital contamination (52), while laser-ablation ICP-MS can target specific mineralogies and components to target marine precipitates and assess potential diagenetic alteration (30). To further filter and identify primary marine samples, we compared REE+Y abundance patterns and ratios to a range of geochemical alteration tracers to assess samples for secondary detrital contamination and diagenetic alteration. For both sequentially leached and laser-ablation results, we found that the cleanest steps for each leach (and the best petrographically preserved components) showed little correlation between Ce/Ce* and Rb/Ca, Mn/Ca, Mn/Sr, Th, Mn, and Mg/Ca. Comparing total REE concentrations in well-preserved samples to Rb, Mn, and Th, we similarly found little correlation (*SI Appendix*, Fig. S7).

Paleoproterozoic Ce/Ce* Depth Gradient

Combining sequential leaching and laser-ablation REE+Y measurements, we found that Pethei Group marine carbonates preserve a range of Ce/Ce* values between 0.8 and 1.5 across the basin. The preservation of moderately depleted Ce anomalies in these marine settings suggests active redox cycling of Ce, where some Ce would have been oxidized and preferentially removed. However, the presence of enriched Ce anomalies (Ce/Ce* >1.0) suggests a relatively shallow chemocline, where sinking Ce-enriched particles would have dissolved deeper in the anoxic water column (22, 23).

Using the sedimentology and stratigraphy of our measured sections to constrain the depositional environment of each sample, we compared Ce/Ce* values between facies. We found that carbonate samples from platform and slope facies preserve a distinctly depleted Ce/Ce* population, with a minor enriched Ce/Ce* population, while deeper basinal facies preserve a large enriched Ce/Ce* population (Fig. 2). The distribution of depleted Ce/Ce* values suggests that Ce reduction was limited to the upper slope and platform environments (i.e., <100 m), although minor enriched Ce/Ce* values suggest occasional mixing events (e.g., storms) could have driven surface waters anoxic for periods of time. The abundance of both highly enriched and mildly depleted Ce anomalies in the slope facies is an excellent indicator that the position of the chemocline, the boundary between oxic and anoxic waters, was restricted to this facies. Above the chemocline, oxic waters would have removed Ce, generating a depleted anomaly, while below the boundary, sinking Ce(IV)-rich particles would have dissolved in anoxic waters, releasing their REE+Y. Deeper basinal carbonates dominantly preserve enriched Ce/Ce* values, consistent with an exclusively anoxic environment. In summary, these results are consistent with the interpretation that the Proterozoic surface ocean was oxic, but based on our facies analysis, that this oxic layer was largely restricted to the upper 50–100 m of the water column.

Modeling Atmospheric pO_2 Using Ce/Ce*

To explore the potential range of paleo-atmospheric pO_2 values necessary to generate the observed Ce/Ce* range in Pethei Group shallow marine carbonates, we developed a Ce oxidation model that combines water-mass residence times from an ocean circulation model with Ce oxidation and particle adsorption rates. We considered several factors, including the depth of the surface oxic layer, water residence times within that layer, and upper-ocean dissolved O_2 concentrations (which are tied to atmospheric pO_2 assuming stable gas-exchange equilibrium and limited influence by local reductant fluxes). We evaluated Ce cycling in a vertical 1D water column bound at its top by the atmosphere, where it is in active air–sea gas exchange, and bound at its base by a chemocline, where dissolved O_2 reaches zero. Similar to modern anoxic basins, the depth of the chemocline would have been tied to physical density stratification, local hydrological mixing rates, and dissolved reductant concentrations, which are all largely unknown. Therefore, we relied on our stratigraphic and geochemical measurements,

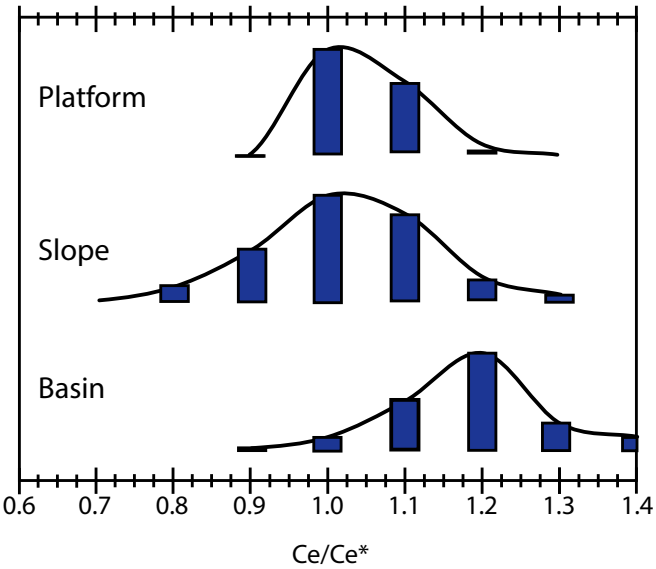

Fig. 2. Ce/Ce* distribution plots for each depositional environment in our sample set (0.1 bin size). Platform and slope facies carbonate samples preserve a relatively depleted Ce/Ce* population (Ce/Ce* <1.0), with a minor enriched Ce/Ce* population (Ce/Ce* >1.0). In comparison, deeper basinal facies preserve a large enriched Ce/Ce* population. This suggests a relatively shallow chemocline at, or slightly above, the boundary between slope and basin facies.

which suggest a relatively shallow chemocline (50–100 m) during Pethei Group deposition, as an independent constraint on chemocline depth. To account for potential uncertainties, we ran three separate models at a range of depths (50, 90, and 169 m).

There is a flux of Ce into the modern surface layer by lithogenic dust fallout, which releases a small but important Ce pool (53), and by the advection of anoxic and REE+Y-rich deep-ocean waters. We used values from global dust models that estimate average deposition of 1–5 g/m^2 per year (54–56) and experimental data that suggest 1.4–2.2% of lithogenic Ce is dissolved and released during the deposition and flocculation of lithogenic dust at the ocean surface (53, 57). Average Ce advection rates at the base of the modeled marine layer are principally driven by water-mass circulation, which varies as the depth of the chemocline (and thus the thickness of the layer) increases. In contrast to most work, which assumes a single or a range of vertical advection rate, we estimated the residence time of water in each depth layer using constraints from an ocean circulation model. Specifically, we used a general circulation model of the modern ocean (IPSL) with the Lagrangian ocean analysis tool Ariane (58, 59) to model the residence time of a given surface ocean layer (*SI Appendix*, Fig. S8). Performing this analysis across various ocean basins and climatic states, we conducted a bootstrap resampling of our results to determine average residence times in the mixed layer of 0.76, 1.70, and 2.46 y for 50-, 90-, and 169-m depths, respectively.

Ce cycling and removal within the modern upper ocean are primarily driven by sorption-desorption of dissolved Ce onto sinking particles (60). Dissolved Ce(III) is actively exchanged with lithogenic dust and organic-matter particle surfaces, and oxidized in a microbially mediated process to insoluble Ce(IV) (25), which immediately binds to particles. We parameterized Ce oxidation rates and particle adsorption ratios using experimental results from Moffett (25, 33), who conducted experiments in multiple sites across a range of dissolved O_2 concentrations. As particle adsorption rates rapidly reach chemical equilibrium (33), Ce removal rates are largely dictated by particle sinking rates. Although particle sinking rates vary greatly and may have been different in the Precambrian (61), we used measured estimates for lithogenic particles in open ocean settings (62, 63), which provide a conservative estimate. We validated our model against observations in the modern Black Sea (*SI Appendix*) but utilized a resampling technique (Monte Carlo) to deal with uncertainties in several key terms and present our results as a range of predicted Ce/Ce* for different atmospheric pO_2 values and chemocline depths (Fig. 3).

Calculating Ce/Ce* values at three chemocline depths across a range of atmospheric pO_2 values (0.05–5%), we found that the maximum Ce/Ce* values of 0.8–0.9 observed in primary phases during the deposition of the Pethei Group are most consistent with atmospheric pO_2 values between ∼0.05 and 1% of the present atmospheric level (PAL). In addition, even at very low atmospheric pO_2 values, deeper chemocline depths generated large Ce/Ce* values (∼0.6 at 0.05% PAL). This strongly suggests a shallow chemocline within 100-m depth in the Pethei basin (Fig. 3). This is in agreement with our depth-constrained Ce/Ce* measurements, and also qualitatively consistent with relatively low atmospheric pO_2 overlying the surface ocean.

Expanding on these model results in the context of the remainder of the Proterozoic, we compiled a REE+Y record from the literature (Fig. 4) to supplement our results from the Pethei Group. Unfortunately, much of the current generation of Ce/Ce* values have not undergone detailed petrographic and geochemical filters and some samples may preserve erroneous and contaminated Ce/Ce* values (31). To provide a first filter, we used neodymium (Nd) anomalies to assess literature samples for potential issues and

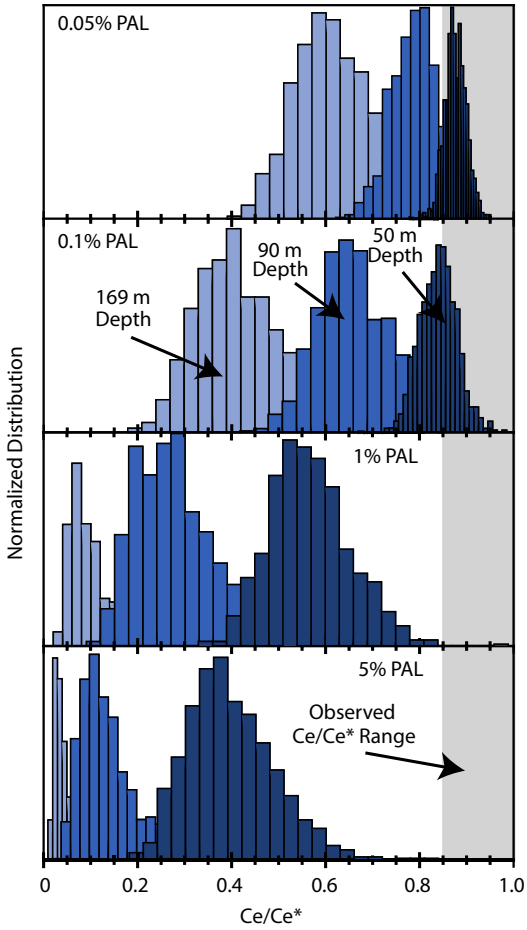

Fig. 3. Model output for different atmospheric pO_2 concentrations at three potential chemocline depths. Consistent with our sedimentological depth estimates (<100 m), our observed Ce/Ce* values of 0.8–0.9 (gray bar) suggest a relatively shallow chemocline (<90 m) and low atmospheric pO_2 values below ∼0.1% PAL during deposition of the Pethei Group.

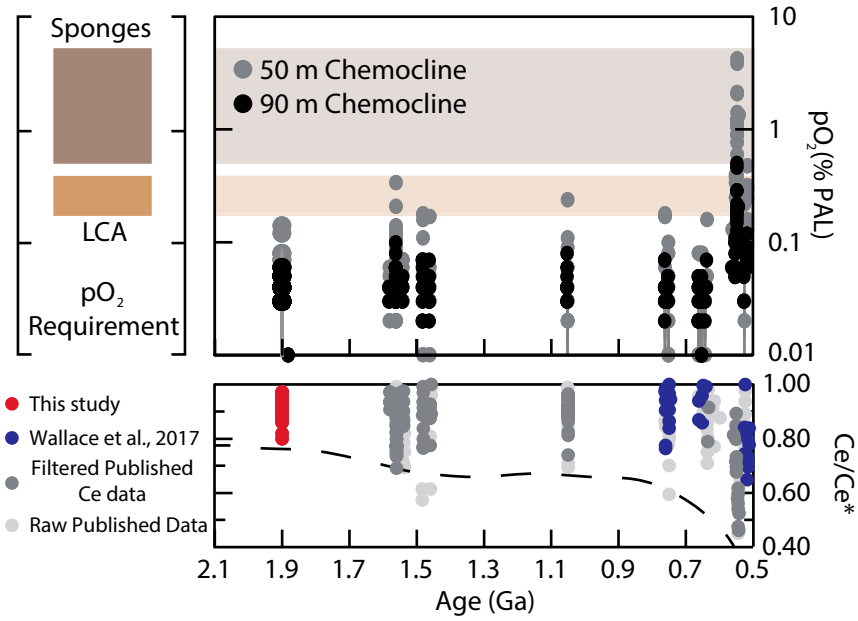

Fig. 4. Using a power function regression of our model outputs to estimate atmospheric oxygen concentrations for our data and literature data, we estimated atmospheric pO_2 assuming a 50- and 90-m-thick chemocline. We compared our results to experimental estimates of sponge O_2 requirements and calculated O_2 requirements for metazoan last common ancestor (LCA) (65, 66). Despite uncertainties in the depth of the chemocline for much of the literature data, our results suggest that before the Ediacaran (~635 Ma), atmospheric pO_2 concentrations were close to the oxygen requirements of basal metazoans. Carbonate Ce/Ce* were taken from this study and from the literature where available (3, 32, 67–71). We filtered data using Nd/Nd* anomalies and did not include Ce/Ce* values from samples with Nd/Nd* offsets of >0.1 from 1.0. LCA, last common ancestor; Nd, neodymium.

ignored samples with large offsets (*SI Appendix*). Despite the risk of potentially problematic Ce/Ce* values, building on the Wallace et al. (3) compilation of the Neoproterozoic, this compilation provides an initial attempt at expanding our approach across the Proterozoic. Using our model output data, we used a power function regression to calculate a pO_2 estimate of each Ce/Ce* value assuming different surface oxic layer thicknesses (Fig. 4*A*).

The Paleo- and Mesoproterozoic carbonate records generally show a relatively narrow range of Ce/Ce* (0.75–1.3), only lowering to more depleted values in the Neoproterozoic (3). Despite the lack of depth constraints for some literature data, these results suggest that much of the early and middle Proterozoic was characterized by maximum pO_2 values between 0.1 and 1% PAL for an oxic layer thickness shallower than 90 or 50 m, respectively. Therefore, following a spike in oxygen at the Lomagundi Event (64), it appears that oxygen levels returned to low values for most of the Proterozoic era and oxic marine conditions were restricted to a thin veneer at the surface ocean. The increasingly greater Ce/Ce* range beginning in the Neoproterozoic (3) likely reflects a combination of a deepening average chemocline depth and increasing atmospheric pO_2 values at this time, which is consistent with previous work (5, 17).

Although there remains considerable debate over the oxygen requirements of early multicellular eukaryotes and how oxygen may have shaped their ecology, our pO_2 estimates fall below current best estimates of metazoan requirements based on experiments using modern sponges and theoretical calculations of metazoan last common ancestor (65, 66). These results are in line with previous work suggesting that low oxygen levels may have been a key factor shaping the ecology and evolution of early animals.

Conclusions

We found evidence for the preservation of a shallow chemocline no more than 50–100 m deep using in situ marine carbonate precipitates of the Paleoproterozoic Pethei Group and a narrow range of Ce/Ce* down to minimum values of ~0.8. Developing a simple Ce oxidation model to explore maximum Ce/Ce* in the upper ocean under different atmospheric pO_2 levels, we estimated that atmospheric pO_2 during the deposition of the Pethei Group was <1% PAL. Extending this across the Proterozoic, these results suggest sustained low atmospheric pO_2 conditions and a shallow marine oxic layer throughout most of the Proterozoic, providing an independent test of current Proterozoic pO_2 estimates. More broadly, this work represents a means to constrain paleo-atmospheric pO_2 using marine carbonates, opening the door to a much denser and detailed pO_2 record than prior black shale or terrestrial paleosol records.

ACKNOWLEDGMENTS. We thank M. Longley, R. Carpenter, A. Besson, S. Leander, T. Kuhn, K. Rybacki, and D. Cole for their assistance in the field. We are grateful to A. Voldoire and R. Séférian for providing the CNRM data and to J. Deshayes for providing the IPSL model data. E.J.B. acknowledges support from the Natural Sciences and Engineering Research Council of Canada (NSERC). A.v.S.H. acknowledges support from a NASA Astrobiology Postdoctoral Fellowship. This work was supported by the Alternative Earths NASA Astrobiology Institute.

1. Canfield DE, Poulton SW, Narbonne GM (2007) Late-Neoproterozoic deep-ocean oxygenation and the rise of animal life. *Science* 315:92–95.
2. Zhang S, et al. (2016) Sufficient oxygen for animal respiration 1,400 million years ago. *Proc Natl Acad Sci USA* 113:1731–1736.
3. Wallace MW, et al. (2017) Oxygenation history of the Neoproterozoic to early Phanerozoic and the rise of land plants. *Earth Planet Sci Lett* 466:12–19.
4. Frei R, Gaucher C, Poulton SW, Canfield DE (2009) Fluctuations in Precambrian atmospheric oxygenation recorded by chromium isotopes. *Nature* 461:250–253.
5. Planavsky NJ, et al. (2014) Earth history: Low mid-Proterozoic atmospheric oxygen levels and the delayed rise of animals. *Science* 346:635–638.
6. Seager S, Deming D (2010) Exoplanet atmospheres. *Annu Rev Astron Astrophys* 48:631–672.
7. Farquhar J, Zerkle AL, Bekker A (2011) Geological constraints on the origin of oxygenic photosynthesis. *Photosynth Res* 107:11–36.
8. Crowe SA, et al. (2013) Atmospheric oxygenation three billion years ago. *Nature* 501:535–538.
9. Kirschvink JL, Kopp RE (2008) Palaeoproterozoic ice houses and the evolution of oxygen-mediating enzymes: The case for a late origin of photosystem II. *Philos Trans R Soc Lond B Biol Sci* 363:2755–2765.
10. Lyons TW, Reinhard CT, Planavsky NJ (2014) The rise of oxygen in Earth's early ocean and atmosphere. *Nature* 506:307–315.

11. Canfield DE (2014) *Oxygen: A Four Billion Year History* (Princeton Univ Press, Princeton, NJ).
12. Pavlov AA, Kasting JF (2002) Mass-independent fractionation of sulfur isotopes in Archean sediments: Strong evidence for an anoxic Archean atmosphere. *Astrobiology* 2:27–41.
13. Segura A, et al. (2003) Ozone concentrations and ultraviolet fluxes on Earth-like planets around other stars. *Astrobiology* 3:689–708.
14. Glasspool IJ, Scott AC (2010) Phanerozoic concentrations of atmospheric oxygen reconstructed from sedimentary charcoal. *Nat Geosci* 3:627–630.
15. Zbinden EA, Holland HD, Feakes CR, Dobos SK (1988) The Sturgeon Falls paleosol and the composition of the atmosphere 1.1 Ga BP. *Precambrian Res* 42:141–163.
16. Sheldon ND (2013) Causes and consequences of low atmospheric pCO2 in the Late Mesoproterozoic. *Chem Geol* 362:224–231.
17. Cole DB, et al. (2016) A shale-hosted Cr isotope record of low atmospheric oxygen during the Proterozoic. *Geology* 44:555–558.
18. Gilleaudeau GJ, et al. (2016) Oxygenation of the mid-Proterozoic atmosphere: Clues from chromium isotopes in carbonates. *Geochem Perspect Lett* 2:178–187.
19. Planavsky NJ, et al. (2016) No evidence for high atmospheric oxygen levels 1,400 million years ago. *Proc Natl Acad Sci USA* 113:E2550–E2551.
20. Lenton TM, Daines SJ (2017) Biogeochemical transformations in the history of the ocean. *Annu Rev Mar Sci* 9:31–58.
21. German CR, Elderfield H (1990) Application of the Ce anomaly as a paleoredox indicator: The ground rules. *Paleoceanography* 5:823–833.
22. German CR, Holliday BP, Elderfield H (1991) Redox cycling of rare earth elements in the suboxic zone of the Black Sea. *Geochim Cosmochim Acta* 55:3553–3558.
23. Bau M, Möller P, Dulski P (1997) Yttrium and lanthanides in eastern Mediterranean seawater and their fractionation during redox-cycling. *Mar Chem* 56:123–131.
24. Bau M, Koschinsky A (2009) Oxidative scavenging of cerium on hydrous Fe oxide: Evidence from the distribution of rare earth elements and yttrium between Fe oxides and Mn oxides in hydrogenetic ferromanganese crusts. *Geochem J* 43:37–47.
25. Moffett JW (1990) Microbially mediated cerium oxidation in sea water. *Nature* 345: 421–423.
26. Taylor SR, McLennan SM (1985) *The Continental Crust: Its Composition and Evolution* (Blackwell, London).
27. Webb GE, Kamber BS (2000) Rare earth elements in Holocene reefal microbialites: A new shallow seawater proxy. *Geochim Cosmochim Acta* 64:1557–1565.
28. Nothdurft LD, Webb GE, Kamber BS (2004) Rare earth element geochemistry of Late Devonian reefal carbonates, Canning Basin, Western Australia: Confirmation of a seawater REE proxy in ancient limestones. *Geochim Cosmochim Acta* 68:263–283.
29. Bau M, Alexander B (2006) Preservation of primary REE patterns without Ce anomaly during dolomitization of mid-Paleoproterozoic limestone and the potential re-establishment of marine anoxia immediately after the "Great Oxidation Event". *S Afr J Geol* 109:81–86.
30. Hood AvS, Wallace MW (2015) Extreme ocean anoxia during the Late Cryogenian recorded in reefal carbonates of southern Australia. *Precambrian Res* 261:96–111.
31. Hood AvS, Planavsky NJ, Wallace MW, Wang X (2018) The effects of diagenesis on geochemical paleoredox proxies in sedimentary carbonates. *Geochim Cosmochim Acta* 232:265–287.
32. Tang D, Shi X, Wang X, Jiang G (2016) Extremely low oxygen concentration in mid-Proterozoic shallow seawaters. *Precambrian Res* 276:145–157.
33. Moffett JW (1994) The relationship between cerium and manganese oxidation in the marine environment. *Limnol Oceanogr* 39:1309–1318.
34. Sami TT, James NP (1996) Synsedimentary cements as Paleoproterozoic platform building blocks, Pethei Group, northwestern Canada. *J Sediment Res* 66:209–222.
35. Hoffman PF (1974) Shallow and deepwater stromatolites in Lower Proterozoic platform–to–basin facies change, Great Slave Lake, Canada. *AAPG Bull* 58:856–867.
36. Sami TT, James NP (1993) Evolution of an early Proterozoic foreland basin carbonate platform, lower Pethei Group, Great Slave Lake, north-west Canada. *Sedimentology* 40:403–430.
37. Sami TT, James NP (1994) Peritidal carbonate platform growth and cyclicity in an early Proterozoic foreland basin, upper Pethei Group, Northwest Canada. *J Sediment Res* 64:111–131.
38. Hotinski RM, Kump LR, Arthur MA (2004) The effectiveness of the Paleoproterozoic biological pump: A δ13C gradient from platform carbonates of the Pethei Group (Great Slave Lake Supergroup, NWT). *Geol Soc Am Bull* 116:539–554.
39. Hoffman PF (1988) East arm of Great Slave Lake, District of Mackenzie, North West Territories. Geological Survey of Canada, Map 1628A (2 sheets), scale 1:250,000 and 1:500,000.
40. Hoffman PF (1989) Pethei reef complex (1.9 Ga), Great Slave Lake, NWT. *Reefs, Canada and Adjacent Areas*, Memoir (Canadian Society of Petroleum Geologists), eds Geldsetzer HHJ, James NP, Tebbutt GE (Canadian Society of Petroleum Geologists, Calgary, Alberta, Canada), Vol 13, pp 33–48.
41. Hoffman PF (1988) United Plates of America, the birth of a craton: Early Proterozoic assembly and growth of Laurentia. *Annu Rev Earth Planet Sci* 16:543–603.
42. Hoffman PF (1987) Continental transform tectonics: Great Slave Lake shear zone (ca. 1.9 Ga), northwest Canada. *Geology* 15:785–788.
43. Johnson BJ (1990) Stratigraphy and structure of the Early Proterozoic Wilson Island Group, East Arm thrust-fold belt, NWT. *Can J Earth Sci* 27:552–569.
44. Bowring SA, Schmus WRV, Hoffman PF (1984) U-Pb zircon ages from Athapuscow aulacogen, East Arm of Great Slave Lake, N.W.T., Canada. *Can J Earth Sci* 21: 1315–1324.
45. van Breemen O, Kjarsgaard B, Tella S, Lemkow D, Aspler L (2013) U-Pb detrital zircon geochronology of clastic sedimentary rocks of the Paleoproterozoic Nonacho and East Arm basins, Thaidene Nene MERA study area. *Mineral and Energy Resource Assessment of the Proposed Thaidene Nene National Park Reserve in the Area of the East Arm of Great Slave Lake, Northwest Territories*, Open File, eds Wright DF, Ambrose EJ, Lemkow D, Bonham-Carter G (Geological Survey of Canada, Ottawa, Ontario, Canada), Vol 7196, pp 119–142.
46. Hoffman PF, Bowring SA, Buchwaldt R, Hildebrand RS (2011) Birthdate for the Coronation paleocean: Age of initial rifting in Wopmay orogen, Canada. *Can J Earth Sci* 48:281–293.
47. Hoffman PF (1973) Evolution of an early Proterozoic continental margin: The Coronation geosyncline and associated aulacogens of the northwestern Canadian shield. *Philos Trans R Soc Lond A* 273:547–581.
48. Jackson M (1988) Early Proterozoic Cowles Lake foredeep reef, NWT, Canada. *Reefs, Canada and Adjacent Areas*, Memoir (Canadian Society of Petroleum Geologists), eds Geldsetzer HHJ, James NP, Tebbutt GE (Canadian Society of Petroleum Geologists, Calgary, Alberta, Canada), Vol 13, pp 64–71.
49. Hoffman P (1967) Algal stromatolites: Use in stratigraphic correlation and paleocurrent determination. *Science* 157:1043–1045.
50. Hoffman PF (1969) Proterozoic paleocurrents and depositional history of the East Arm fold belt, Great Slave Lake, Northwest Territories. *Can J Earth Sci* 6:441–462.
51. Pope MC, Grotzinger JP (2000) Controls on fabric development and morphology of tufas and stromatolites, uppermost Pethel Group (1.8 Ga), Great Slave Lake, northwest Canada. *Carbonate Sedimentation and Diagenesis in the Evolving Precambrian World*, SEPM Special Publication, eds Grotzinger JP, James NP (SEPM, Tulsa, OK).
52. Tostevin R, et al. (2016) Effective use of cerium anomalies as a redox proxy in carbonate-dominated marine settings. *Chem Geol* 438:146–162.
53. Pearce CR, Jones MT, Oelkers EH, Pradoux C, Jeandel C (2013) The effect of particulate dissolution on the neodymium (Nd) isotope and rare earth element (REE) composition of seawater. *Earth Planet Sci Lett* 369–370:138–147.
54. Mahowald NM, et al. (2005) Atmospheric global dust cycle and iron inputs to the ocean. *Global Biogeochem Cycles* 19:GB4025.
55. Kok JF, et al. (2017) Smaller desert dust cooling effect estimated from analysis of dust size and abundance. *Nat Geosci* 10:274–278.
56. Han Q, Moore JK, Zender C, Measures C, Hydes D (2008) Constraining oceanic dust deposition using surface ocean dissolved Al. *Global Biogeochem Cycles* 22:GB2003.
57. Greaves MJ, Statham PJ, Elderfield H (1994) Rare earth element mobilization from marine atmospheric dust into seawater. *Mar Chem* 46:255–260.
58. Blanke B, Raynaud S (1997) Kinematics of the Pacific equatorial undercurrent: An Eulerian and Lagrangian approach from GCM results. *J Phys Oceanogr* 27:1038–1053.
59. Thomas MD, Fedorov AV (2017) The eastern subtropical Pacific origin of the equatorial cold bias in climate models: A Lagrangian perspective. *J Clim* 30:5885–5900.
60. Schijf J, Christenson EA, Byrne RH (2015) YREE scavenging in seawater: A new look at an old model. *Mar Chem* 177:460–471.
61. Planavsky NJ, et al. (2015) Late Proterozoic transitions in climate, oxygen, and tectonics, and the rise of complex life. *Earth-Life Transitions: Paleobiology in the Context of Earth System Evolution*, eds Polly PD, Head JJ, Fox DL (Paleontological Society, Boulder, CO), Vol 21, pp 47–82.
62. Bressac M, et al. (2012) A mesocosm experiment coupled with optical measurements to assess the fate and sinking of atmospheric particles in clear oligotrophic waters. *Geo-Mar Lett* 32:153–164.
63. Collins JR, et al. (2015) The multiple fates of sinking particles in the North Atlantic Ocean. *Global Biogeochem Cycles* 29:1471–1494.
64. Blättler C, et al. (2018) Two-billion-year-old evaporites capture Earth's great oxidation. *Science* 360:320–323.
65. Mills DB, et al. (2014) Oxygen requirements of the earliest animals. *Proc Natl Acad Sci USA* 111:4168–4172.
66. Sperling EA, Halverson GP, Knoll AH, Macdonald FA, Johnston DT (2013) A basin redox transect at the dawn of animal life. *Earth Planet Sci Lett* 371–372:143–155.
67. Azmy K, Sylvester P, de Oliveira TF (2009) Oceanic redox conditions in the late Mesoproterozoic recorded in the upper Vazante Group carbonates of São Francisco Basin, Brazil: Evidence from stable isotopes and REEs. *Precambrian Res* 168:259–270.
68. Huang J, Chu X, Jiang G, Feng L, Chang H (2011) Hydrothermal origin of elevated iron, manganese and redox-sensitive trace elements in the c. 635 Ma Doushantuo cap carbonate. *J Geol Soc London* 168:805–816.
69. Ling H-F, et al. (2013) Cerium anomaly variations in Ediacaran–earliest Cambrian carbonates from the Yangtze Gorges area, South China: Implications for oxygenation of coeval shallow seawater. *Precambrian Res* 225:110–127.
70. Hua G, et al. (2013) Trace and rare earth elemental geochemistry of carbonate succession in the Middle Gaoyuzhuang Formation, Pingquan Section: Implications for Early Mesoproterozoic ocean redox conditions. *J Palaeogeogr* 2:209–221.
71. Khelen AC, et al. (2017) Geochemical and stable isotope signatures of Proterozoic stromatolitic carbonates from the Vempalle and Tadpatri Formations, Cuddapah Supergroup, India: Implications on paleoenvironment and depositional conditions. *Precambrian Res* 298:365–384.